European Journal of Pharmaceutical Sciences 134 (2019) 256–265

Contents lists available at ScienceDirect

European Journal of Pharmaceutical Sciences

journal homepage: www.elsevier.com/locate/ejps

Selective redox-responsive theragnosis nanocarrier for breast tumor cells mediated by MnO_2/fluorescent carbon nanogel

Cheong A Choi[a,1], Benny Ryplida[b,1], Insik In[b,c], Sung Young Park[a,b,*]

[a] Department of Chemical and Biological Engineering, Korea National University of Transportation, Chungju 380-702, Republic of Korea
[b] Department of IT Convergence, Korea National University of Transportation, Chungju 380-702, Republic of Korea
[c] Department of Polymer Science and Engineering, Korea National University of Transportation, Chungju 380-702, Republic of Korea

ARTICLE INFO

Keywords:
Redox-responsive nanogel
Hyaluronic acid
Carbon dot
MnO_2 nanosheet
Targeted drug delivery

ABSTRACT

A redox-responsive fluorescent carbon nanogel (FCN) was designed as a bioimaging probe for targeted drug delivery to cancer cells. FCN was synthesized by the carbonization of disulfide cross-linked hyaluronic acid in the fluorescence "on" mode, followed by the attachment of manganese oxide (MnO_2) nanosheets for fluorescence quenching (fluorescence "off"). We hypothesized that the fluorescence intensity of paclitaxel (PTX)-MnO_2/FCN would suddenly increase (fluorescence "on") in the presence of a high level of glutathione (GSH) in cancer cells, owing to the reduction of MnO_2 to Mn^{2+} and cleavage of the disulfide bond. Consequently, PTX would be released from the FCN system. Consistent with this hypothesis, the designed system recovered FCN fluorescence and triggered drug release through the cleavage of the disulfide bond by GSH. Moreover, PTX-MnO_2/FCN demonstrated stable fluorescence intensity after GSH treatment, serving as a potential biosensor. PTX-MnO_2/FCN exhibited excellent biocompatibility with normal cells and selectively targeted tumor cells, highlighting the therapeutic capabilities of this system. The developed PTX-MnO_2/FCN structure may serve as a smart drug delivery system with diagnostic and therapeutic properties, good selectivity, and compatibility, and with excellent potential for biomedical applications.

1. Introduction

Cancer, one of the leading causes of death, is a dangerous disease that poses a challenge to researchers worldwide to actively develop relevant approaches for improvement in therapeutic outcomes. Drug delivery systems (DDSs) have the potential to enhance therapeutic effectiveness, particularly through their targeting properties, biocompatibility, biodegradability, and efficient drug release (Ghaffaro et al., 2018; Al-Nahain et al., 2013; Wang et al., 2018). The environmental conditions within tumor cells are different from those of normal cells in terms of pH, enzyme level, and redox potential. This difference may be exploited for the detection, targeting, or control of drug release from DDSs.

A stimulus-responsive polymer nanogel based on hyaluronic acid (HA) has been extensively studied for the development of a targeted drug delivery matrix. Attributes of the nanogel include suitable particle size, high drug loading efficiency, good colloidal stability, and excellent biocompatibility (Ossipov et al., 2010). HA-based derivatives have also been investigated for their cell imaging capabilities for cancer diagnosis through the interaction between HA molecules and CD44, conjugated using quantum dots or organic fluorescent dyes, such as fluorescein, to optimize tracking properties. Despite these advantages, HA in its pure form lacks fluorescence activity, has poor biomechanical properties, and is easily degraded, thereby limiting its application as a controlled DDS (Choh et al., 2011; Huang et al., 2014; Pedrosa et al., 2014). However, in 2015, Park et al. successfully synthesized *in situ* luminescence carbon nanoparticles by carbonization of the pure form of HA as a tumor-targeting bioimaging matrix (Sharker et al., 2015). Fluorescent carbon dots have now emerged as the first-choice luminescence nanomaterials, given their ease of preparation, low toxicity, high quantum yield, excellent biocompatibility, and good photostability, and have been widely used for bioimaging and as biosensors, catalysts, and optoelectronic devices (An et al., 2002; Ding et al., 2014). Carbon dots may be used for visual detection based on the surrounding environmental conditions. All these properties make carbon dots suitable biosensors, owing to the convenience of the fluorescence "off/on" system (Sun and Lei, 2017). Moreover, the hydrophobic properties of carbon dots facilitate the loading of drugs *via* hydrophobic interactions (Chowdhuri

* Corresponding author at: Department of Chemical and Biological Engineering, Korea National University of Transportation, Chungju 380-702, Republic of Korea.
E-mail address: parkchem@ut.ac.kr (S.Y. Park).
[1] These authors equally contributed to this work.

https://doi.org/10.1016/j.ejps.2019.04.027
Received 19 November 2018; Received in revised form 25 March 2019; Accepted 27 April 2019
Available online 29 April 2019
0928-0987/

et al., 2015). Despite these advantages, further modifications of carbon dots are warranted, particularly to improve their selectivity and therapeutic abilities. Manganese oxide (MnO_2) nanosheets display excellent drug delivery capabilities by acting as a quencher by Förster resonance energy transfer (FRET) and as a redox potential sensor, owing to the reduction of MnO_2 to Mn^{2+} (Wang et al., 2015). Cancer cells contain glutathione (GSH) in intracellular compartments at a concentration of approximately 2–10 mM, which is about four times higher than that in normal cells. GSH reduces MnO_2, which serves as a marker of the targeting properties of the MnO_2 nanosheet (Meng et al., 2009; Chen et al., 2017). As it is difficult to use HA for *in situ* fluorescence bioimaging due to the inability to control the loading and release of the drug, we hypothesized that the modified fluorescent nanogel based on the disulfide-crosslinked HA and labeled with a MnO_2 nanosheet for fluorescence quenching may serve as a selective bioimaging material and drug carrier.

To explore this hypothesis, we synthesized a paclitaxel (PTX)-loaded redox-responsive fluorescent carbon nanogel (FCN) based on disulfide cross-linked HA encapsulated by MnO_2 nanosheets with a redox-responsive fluorescence "off/on" system and evaluated its application for tumor bioimaging and therapy. The incorporation of a disulfide bond in the carbonized cross-linked HA nanogel may impart controllable release behavior and redox-responsive properties, which would activate the fluorescence "off/on" system and allow the controlled release of PTX in the GSH-rich tumor environment. The attachment of MnO_2 to FCN may further increase the system sensitivity due to fluorescence quenching and enhance the response to GSH. The GSH-mediated reduction may remove MnO_2 from the FCN surface while simultaneously cleaving the disulfide bond to release PTX from FCN. As a consequence, this process may increase the detection selectivity and drug release efficiency and maintain biodegradability for efficient targeting and bioimaging.

2. Experimental section

2.1. Materials and characterization

We obtained HA (molecular weight [MW] = 230 kDa) from LifeCore. Cysteamine dihydrochloride, potassium permanganate ($KMnO_4$) solution, 2-(N-morpholino)ethanesulfonic acid (MES) buffer, PTX, GSH, N-(3-dimethylaminopropyl)-N-ethylcarbodiimide hydrochloride (EDC), N-hydroxysuccinimide (NHS), concentrated sulfuric acid (H_2SO_4), and ethanol were purchased from Sigma–Aldrich, Korea. Phosphate-buffered saline (PBS) was supplied by Bioneer Corp., Korea. Roswell Park Memorial Institute (RPMI)-1640 medium, fetal bovine serum (FBS), trypsin-ethylenediaminetetraacetic acid (trypsin-EDTA, 0.03% w/v), and penicillin–streptomycin were procured from Gibco BRL. Fluorescein isothiocyanate (FITC) Annexin-V, propidium iodide (PI), LysoTracker Green DND-26, and MitoTracker Red CMXRos were obtained from Life Technologies.

^{1}H nuclear magnetic resonance (NMR) characterization was performed using the Bruker Avance 400 MHz spectrometer with deuterium oxide (D_2O). The ultraviolet-visible (UV–vis) data were obtained using and Optizen 2020UV spectrometer (Mecasys Co.) and fluorescence emission spectra were recorded using a model L550B luminescence spectrometer (PerkinElmer). The hydrodynamic diameter was recorded using a Zetasizer Nano device (Malvern). X-ray photoelectron spectroscopy (XPS) spectra were obtained with an Omicrometer ESCALAB apparatus (Taunusstein). The 3-(4,5-dimethylthiazol-2-Yl)-2,5-diphenyltetrazolium bromide (MTT) viability assay was performed using a FilterMax F3 microplate reader (Molecular Devices). Flow cytometry was conducted using an Attune NxT Acoustic Focusing Cytometer (Life Technologies). Transmission electron microscopy (TEM) imaging was carried out using a JEM-2100F microscope (JEOL). Confocal microscopy images were recorded with an LSM510 confocal microscope (Carl Zeiss).

2.2. Carbonization of a redox-responsive FCN from disulfide-crosslinked HA (HA-S-S-HA)

FCN was synthesized with the following protocol. First, 1 g HA was dissolved in 50 mL of 2× PBS (pH 3.05) solution, followed by the addition of molar excess of EDC, NHS, and cysteamine dihydrochloride. The reaction was allowed to proceed for 24 h at 24 °C, and the solution was dialyzed against water overnight using a membrane with a MW cut-off of 1 kDa. The solution was freeze-dried and designated as HA-S-S-HA.

HA-S-S-HA (0.25 g) was dissolved in 5 mL deionized water and stirred at 300 rpm. After complete solubilization, the solution was treated with the slow addition of 10 mL of H_2SO_4 and stirred for 1 min. The mixture was poured into deionized water and purified by dialysis (MW 1 kDa) against water. The final solution was freeze-dried and designated as FCN.

2.3. MnO_2 loading into FCN

Approximately 10 mg of FCN was added to 1 mL of deionized water and treated with 10 mL of 0.1 M MES buffer (pH 6.0) followed by sonication for 30 min. To load MnO_2, 5 mM $KMnO_4$ was added and the mixture was centrifuged at 4000 rpm for 15 min. The pellet was repeatedly washed with double-distilled water and the collected sample was freeze-dried and designated as MnO_2/FCN.

2.4. PTX loading into MnO_2/FCN and release kinetics of PTX from PTX-MnO_2/FCN

PTX loading was achieved by mixing approximately 5 mg/mL of PTX dissolved in ethanol and 100 mg of MnO_2/FCN in PBS (pH 7.4), followed by vigorous stirring for 24 h in the dark. To remove unloaded PTX, the solution was centrifuged at 4000 rpm for 10 min. The solvent was completely removed, and the solution was freeze-dried and designated as PTX-MnO_2/FCN. PTX loading (%LC) and encapsulation efficiency (%EE) were calculated based on UV–vis absorbance. The absorbance peak at 480 nm wavelength was detected with a UV spectrophotometer using the following equations (Hu et al., 2015a; Cabeza et al., 2017):

$$\%LC = (\text{mass of drug loaded in nanoparticles} \times 100) / \text{mass of drug loaded nanoparticles}$$

$$\%EE = (\text{weight of PTX in nanoparticles} \times 100)/\text{weight of PTX in Feed}$$

The release profile of PTX from PTX-MnO_2/FCN was analyzed at different concentrations of GSH (0, 3, 6, and 10 mM) inside the dialysis chamber immersed in a release solution (PBS 7.4, approximately 30 mL). The treated samples were placed inside a shaking incubator at 37 °C and the absorbance of the surrounding solution was analyzed using UV–vis spectrophotometry to determine the amount of released PTX.

2.5. Cytotoxicity assay

To analyze cell viability, MDCK and MDA-MB-231 cells at a density of 2×10^5 cells/mL were cultured overnight in 96-well plates (200 μL/well) in a 37 °C incubator with a humidified 5% CO_2 atmosphere. The stock solution of PTX-MnO_2/FCN was prepared in RPMI-1640 medium (1 mg/mL) and serially diluted to 0.001 mg/mL. The cells media was taken out, replaced with stocked solution, and incubated further. After 24 h incubation, the medium was removed, MTT solution was added, and the plate was incubated for 4 h. The MTT solubilization solution (200 μL) was added after removal of the medium and shaken for 15 min. Absorbance was measured using a microplate reader at a wavelength of 570 nm. The relative viability of treated cells was calculated

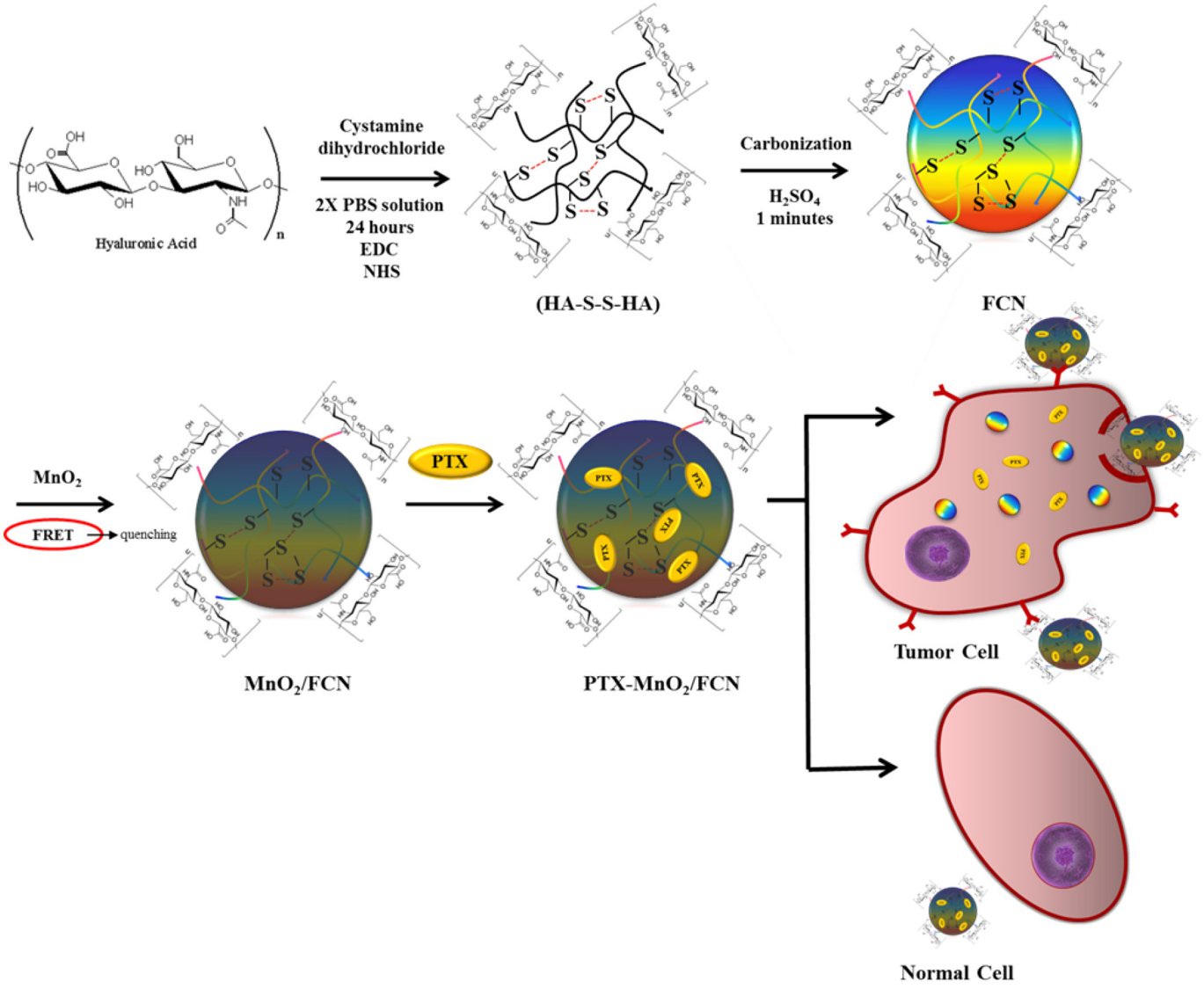

Scheme 1. Schematic diagram of the PTX-loaded redox-controlled luminescence "off/on" system based on MnO_2-loaded fluorescent carbon nanogel for tumor-targeted delivery.

and compared with that of the control cells.

2.6. Flow cytometry

MDCK and MDA-MB-231 cells were cultured in six-well plates at a density of 1×10^6 cells/mL per well in a humidified incubator with an atmosphere of 5% CO_2 for 24 h at 37 °C. After incubation, the medium was replaced with a solution of PTX-MnO_2/FCN dissolved in the medium and the cells were incubated for the designated time. After incubation, the cells were treated with 1% FBS in PBS (pH 7.4) and analyzed using an Attune NxT Acoustic Focusing Cytometer at an excitation wavelength of 405 nm and emission wavelength of 440/50 nm. For the analysis of apoptosis, the cells were immediately analyzed after staining with Annexin-V and PI using an excitation wavelength of 488 nm and an emission wavelength of 530/30 nm and 574/26 nm, respectively.

2.7. Confocal imaging

The cellular uptake of the particles was analyzed using confocal imaging. MDCK and MDA-MB-231 cells were cultured in eight-well plates (1×10^5 cells/mL per well) in an incubator with a humidified 5% CO_2 atmosphere at 37 °C for 24 h. The cells were then treated with PTX-MnO_2/FCN (1 mg/mL) dissolved in medium for 30 min, 1 h, 2 h, 4 h, or 6 h. The medium was then removed, and the cells were washed several times with PBS (pH 7.4) to remove any unbound PTX-MnO_2/FCN and stained with 50 nM LysoTracker Green (acidic compartment) for 30 min. The cells were washed again with PBS and 50 nM SYTO 61 was added to stain nucleic acid for 15 min. The cells were washed with PBS and cell medium was added. The time-dependent internalization was observed with a model LSM510 confocal laser-scanning microscope (magnification 20×) using appropriate filters for FCN (excitation 340 nm, emission 360 nm), LysoTracker Green (excitation 504 nm, emission 511 nm), and SYTO 61 (excitation 628 nm, emission 645 nm) (Cabeza et al., 2017; Liaskoni et al., 2018).

For live/dead cell analysis, cell imaging was performed using calcein-AM and PI staining. MDCK and MDA-MB-231 cells were incubated in eight-well plates at 37 °C in the presence of PTX-MnO_2/FCN (0.2 mg/mL) for 3 h. The prepared cells were stained with calcein-AM and PI and imaged with a LSM510 confocal laser-scanning microscope (magnification, 10×) to quantify the stained cells (live or dead).

2.8. Power analysis

Statistical analysis for cell viability was performed by G*Power 3 software using *t*-tests Post-hoc power analysis with the following inputs: Tail(s) = Two; Effect size d = 3.149519; α error probability = 0.05; sample size group 1 = 3, sample size group 2 = 3.

3. Results

3.1. Synthesis and characterization of redox-controlled fluorescent "off-on" PTX-MnO_2/FCN

HA is a polymer with excellent biocompatibility, and around 50% of the total HA content of the body is present in the skin. However, HA is difficult to use for *in situ* fluorescence bioimaging and may not allow control of drug loading and release. We hypothesized that the modified fluorescent nanogel based on the disulfide-crosslinked HA may have desirable properties for bioimaging and drug delivery. With the coupling of the MnO_2 nanosheet, FRET may make the system more selective and allow control over the fluorescence "off/on" system upon exposure to high concentrations of GSH. To develop a smart drug delivery matrix for the creation of a redox-responsive DDS with therapeutic capabilities, HA was modified using a disulfide bond and carbonized to obtain HA-based FCN. The disulfide bond acted as a crosslinker and maintained the stability of the structure to facilitate drug loading and imparted a redox-responsive property. To enhance the redox-responsive capabilities and selectivity, MnO_2 was loaded onto the cross-linked FCN to fabricate a fluorescence "off/on" nanogel system (Wang et al., 2015; Meng et al., 2009; Chen et al., 2017; Li et al., 2011). The fluorescence is turned "off" after the loading of MnO_2 nanosheets and is turned "on" in response to high GSH concentrations. Thus, this system functions as a potential redox-responsive sensor by reducing MnO_2 to Mn^{2+} (Chen et al., 2014). The crosslinking site in this nanocarrier may, therefore, regulate the selectivity to GSH to deliver PTX specifically to tumor sites. The detailed synthesis process of the redox-responsive FCN for theragnosis applications as a targeted DDS with enhanced drug delivery efficiency and cancer bioimaging properties is illustrated in Scheme 1.

The structure of the DDS was confirmed by ^{1}H NMR spectroscopy as shown in Fig. 1(a). The data demonstrated the difference in PTX profile before and after treatment with 10 mM GSH. Aromatic peaks at 7.5–8 ppm were present after the loading of PTX but disappeared after GSH treatment, indicative of the release of the drug (Kim et al., 2018). The peak at 3.5–4.5 ppm, representing HA, was sharper in the absence of the drug but was lower in the presence of PTX, demonstrating the successful loading and unloading of PTX (Kim et al., 2017). For further investigation, UV–vis spectroscopy was used to characterize absorption properties. As shown in Fig. 1(b), the broad UV–vis absorption spectra of MnO_2 nanosheets could be recognized at approximately 360–550 nm. After PTX loading, a new absorbance peak was observed at 250 nm, which suggested PTX attachment. The overall absorbance increased after drug loading, indicating that PTX was attached to the DDS but had no influence on the MnO_2 absorbance peak (Kim et al., 2017; Ou et al., 2017). In addition, the fluorescence properties were investigated using photoluminescence spectroscopy. FCN was confirmed as a luminescence material, as evident from the high photoluminescence (PL) intensity peak in Fig. 1(c). However, the fluorescence intensity suddenly dropped due to the quenching effect from MnO_2 FRET, which set the overall system into the fluorescence "off" state (Wang et al., 2015). The PL spectrum of PTX-MnO_2/FCN remained low, indicating that PTX had no influence on the fluorescence of the material. After GSH treatment, the fluorescence of the system was turned "on" owing to GSH reactivity that reduced MnO_2 to Mn^{2+}. Hence, the MnO_2 quenching effect vanished while simultaneously breaking down the disulfide bond to increase the signal intensity, reflective of the opening of the FCN structure (Meng et al., 2009). The increase in the fluorescence signal after GSH treatment indicated the cleavage of the disulfide bond of FCN, consistent with the decrease in the particle size of FCN. The surface area of FCN was elevated, which enhanced the emission intensity (Mazrad et al., 2018). PTX-MnO_2/FCN displayed a decay time of 3.3 ns, as evident from the quenching effect by FRET. However, GSH treatment extended the lifetime of the nanogel to 13.0 ns, indicative of the fluorescence switch "on" behavior, as demonstrated in Fig. 1(d).

Size is an important aspect that determines the theragnostic properties of a DDS and its behavior in circulation. Successful intravenous delivery necessitates the use of nanoparticles with sizes below 300 nm (Gupta, 2016; Danaei et al., 2018). Therefore, dynamic light scattering (DLS) analysis was used to quantify the hydrodynamic diameter of FCN, MnO_2/FCN, and PTX-MnO_2/FCN. The results are shown in Fig. 2(a). FCN samples exhibited a particle size of approximately 123.1 nm, which increased to 169.1 nm after the attachment of the MnO_2 nanosheets to the FCN matrix. After PTX loading, the size further increased to 189 nm because of the aggregation of drug molecules and matrix *via* the hydrophobic interaction between PTX and FCN. As shown in Fig. S1, the zeta potential of FCN in PBS 7.4 was −16.17 mV, which became more negative after the attachment of MnO_2 and PTX in MnO_2/FCN and PTX-MnO_2/FCN (−20.35 and −23.99 mV, respectively). The morphological structures of FCN, MnO_2/FCN, and PTX-MnO_2/FCN after GSH treatment were observed by TEM, as shown in Fig. 2(b). Attachment of MnO_2 nanosheets to the FCN structure could be clearly differentiated. FCN displayed a spherical shape with a 0.25 nm lattice spacing that changed to a layer-like form after the attachment of MnO_2. The FCN lattice structure was retained, which was attributable to the encapsulation of FCN by MnO_2 Treatment with GSH reduced the particle size due to the cleavage of the disulfide bonds and opening of the structure by GSH. The structure of FCN was similar to that of a graphene lattice, as most of the lattice spacing was 0.33 nm. To explain the redox-responsive behavior, XPS was conducted. The XPS wide-scan spectra of PTX-MnO_2/FCN before and after GSH treatment showed peaks at 285 and 400 eV (Fig. 2(c)), which were specific to C and O elements, respectively. Furthermore, Mn 2p peaks appeared in untreated PTX-MnO_2/FCN. The GSH environment affected MnO_2 nanosheets by reducing MnO_2 to Mn^{2+} *via* an electron-exchange mechanism, as evident from the disappearance of Mn 2p peaks at 630–660 eV, indicative of the release of MnO_2 nanosheets from FCN (Gupta, 2016). Moreover, the S 2p survey indicated that GSH treatment also cleaved the disulfide bonds, as evident from the decrease in the binding energy from 164 eV (specific to S−S bond) to 162 eV, which is specific to S−H bonds (Castner, 1996). In contrast, the C 1s XPS narrow scan spectra for DDS before and after GSH treatment revealed peaks at 283, 284.3, 284.6, and 288.3 eV, reflecting the C=C, C=N, C−C, and O-C=O peaks, respectively. C=C was the highest peak, indicating that most of the FCN structures contained carbon double bonds. Overall, XPS analysis determined the structure of MnO_2/FCN and PTX-MnO_2/FCN species and confirmed MnO_2 reduction and disulfide cleavage in the presence of GSH.

3.2. PTX loading into MnO_2/FCN and release kinetics of PTX from PTX-MnO_2/FCN

For a better understanding of redox sensitivity, FL spectra and DLS histograms of FCN, MnO_2/FCN, and PTX-MnO_2/FCN at different GSH concentrations and time points were analyzed. As shown in Fig. S2, the FCN size reduced, and its fluorescent intensity slightly increased after the addition of GSH, indicative of the cleavage of disulfide bonds in the FCN system. In contrast, MnO_2/FCN showed distinguished phenomena in the presence of different concentrations of GSH, as displayed in Fig. 3(a). After treatment with 10 mM GSH, the size of MnO_2/FCN decreased from 170 to 100 nm during the first 2 h and remained stable until 24 h because of the complete cleavage of the disulfide bond and reduction of MnO_2 nanosheets. The size of PTX-MnO_2/FCN was similarly reduced from 200 to 100 nm in 2 h and was maintained for 24 h.

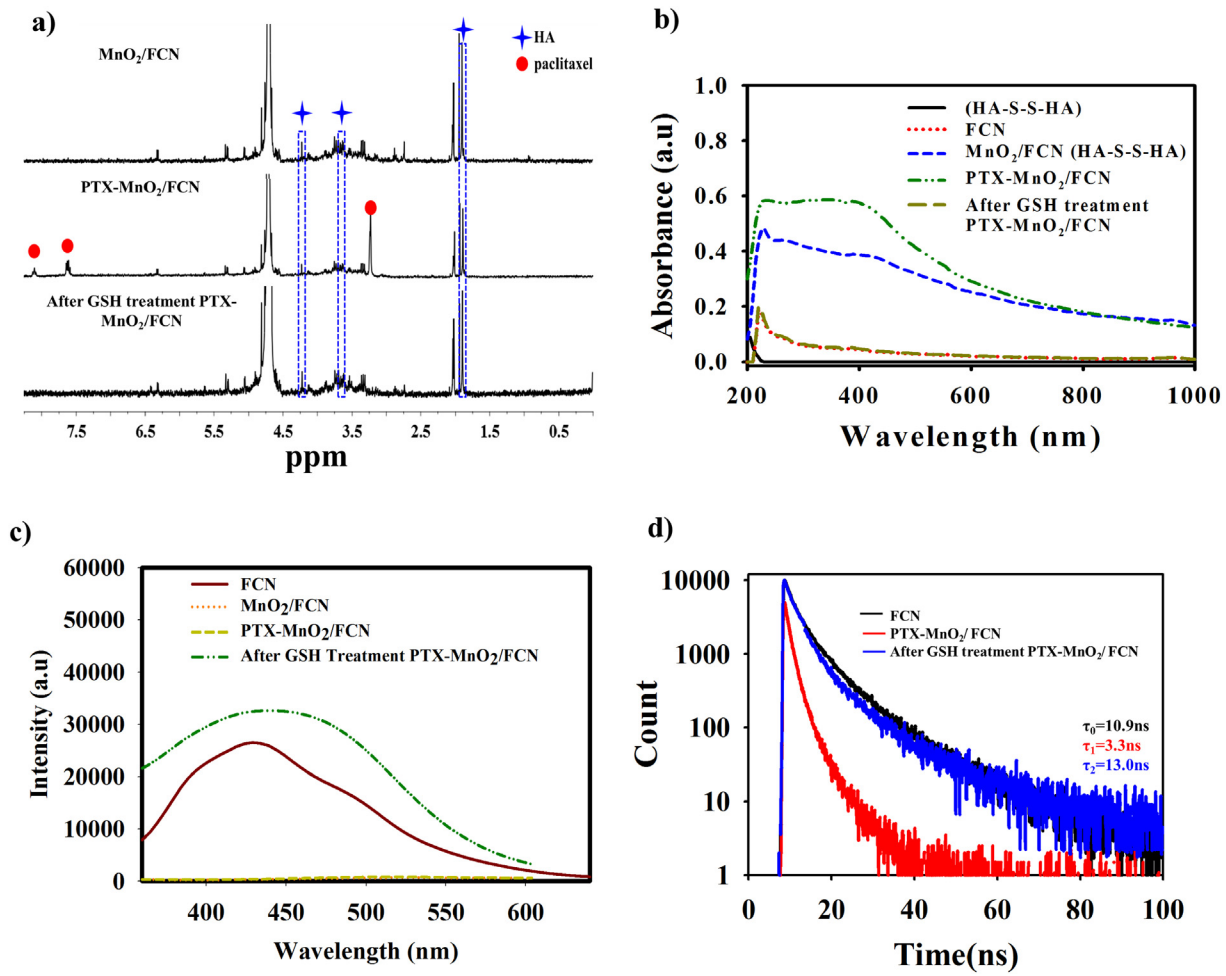

Fig. 1. (a) ^{1}H NMR spectra (400 MHz, DMSO-d_6) of MnO_2/FCN (upper panel), PTX-MnO_2/FCN (middle panel), and PTX-MnO_2/FCN after GSH (10 mM) treatment (lower panel). (b) UV–vis absorption spectra and (c) PL spectra of FCN, MnO_2/FCN, and PTX-MnO_2/FCN, as well as PTX-MnO_2/FCN after treatment with 10 mM GSH (Ex 340 nm, Em 360 nm). (d) Fluorescence lifetime curve of the synthesized drug delivery system at a wavelength of 350 nm (n = 3).

MnO_2/FCN detection properties indicated a remarkable performance (Fig. 3(c)). At 0 mM GSH, the fluorescence was completely "off", even at 24 h, which explains the structural stability of the molecule. However, the fluorescence intensity started to increase after treatment with GSH because of the release of MnO_2 and cleavage of disulfide bonds, especially within the first 5 h. The intensity slightly increased after 5 h until 24 h, which indicated the stability of the fluorescence. Despite PTX loading, PTX-MnO_2/FCN showed good detection behavior, given that the fluorescence of the system was completely quenched in the absence of GSH and was eventually switched "on" in the presence of GSH and remained stable until 24 h.

To investigate the response to stimuli, the drug release profile was monitored using UV–vis spectroscopy by examining the change in absorbance over time (Kang et al., 2017). The PTX-MnO_2/FCN loading (% LC) and encapsulation efficiency (%EE) were 2.9731% and 94.0350%, respectively. The release of PTX from the PTX-MnO_2/FCN matrix in the presence of different concentrations of GSH was investigated (Fig. 4(a)). PTX was entrapped and failed to be released from the MnO_2/FCN system in the absence of GSH due to the lack of the reduction-oxidation reaction between MnO_2 and GSH, as well as the cleavage of disulfide bonds. However, the increase in the concentration of GSH resulted in a gradual increase in drug release. Approximately 80% of the drug was delivered within 5 h after treatment with 10 mM of GSH. This result indicated the opening of MnO_2 layers and the cleavage of the disulfide bond of PTX-MnO_2/FCN (Hu et al., 2015b). Most DDSs rely on the use of dyes, such as fluorescent dyes (either conjugated or loaded into the matrices), for breast cancer cell diagnosis. However, the PTX-MnO_2/FCN system exhibited the fluorescence "off/on" behavior without the use of dyes and showed excellent redox-responsive fluorescence emission after exposure to the GSH level reported in breast cancer cells. In addition, the system had a higher encapsulation efficiency than the reported micelle or polymeric drug carriers and also had excellent sensitivity toward GSH (Tripodo et al., 2015; Zhang and Feng, 2006; Peng et al., 2016). To determine the uptake behavior, flow cytometry analysis was performed. MDCK and MDA-MB-231 cells were first evaluated without treatment, as shown in Fig. 4. Among the several cell types available, three kinds of cells are frequently used for breast cancer cells research—MCF7, T47D, and MDA-MB-231 (Dai et al., 2017). Of these three, MDA-MB-231 cells displayed better internalization of HA-based nanoparticles due to the overexpression of CD44, which is a surface marker and transmembrane hyaluronan receptor (Yang et al., 2015; Youm et al., 2014). Moreover, to confirm the HA system behavior, validation using one normal cell line and one cancer cell line has been previously reported (Youm et al., 2014; Kong et al., 2018; Zhang et al., 2018). Based on this information, MDCK and MDA-MB-231 cells were chosen for an *in vitro* analysis (Smith and Cai, 2012). At 0 mM GSH, PTX-MnO_2/FCN treatment of MDCK cells displayed no shift in signal intensity, which explained the material quenching state in normal cells (Fig. 4(b)). However, MDA-MB-31 cells treated with PTX-MnO_2/FCN demonstrated an increase in fluorescence intensity, as presented in Fig. 4(c), indicating that the nanomaterials were bound to MDA-MB-31 cells. The FCN derived from the disulfide-crosslinked HA

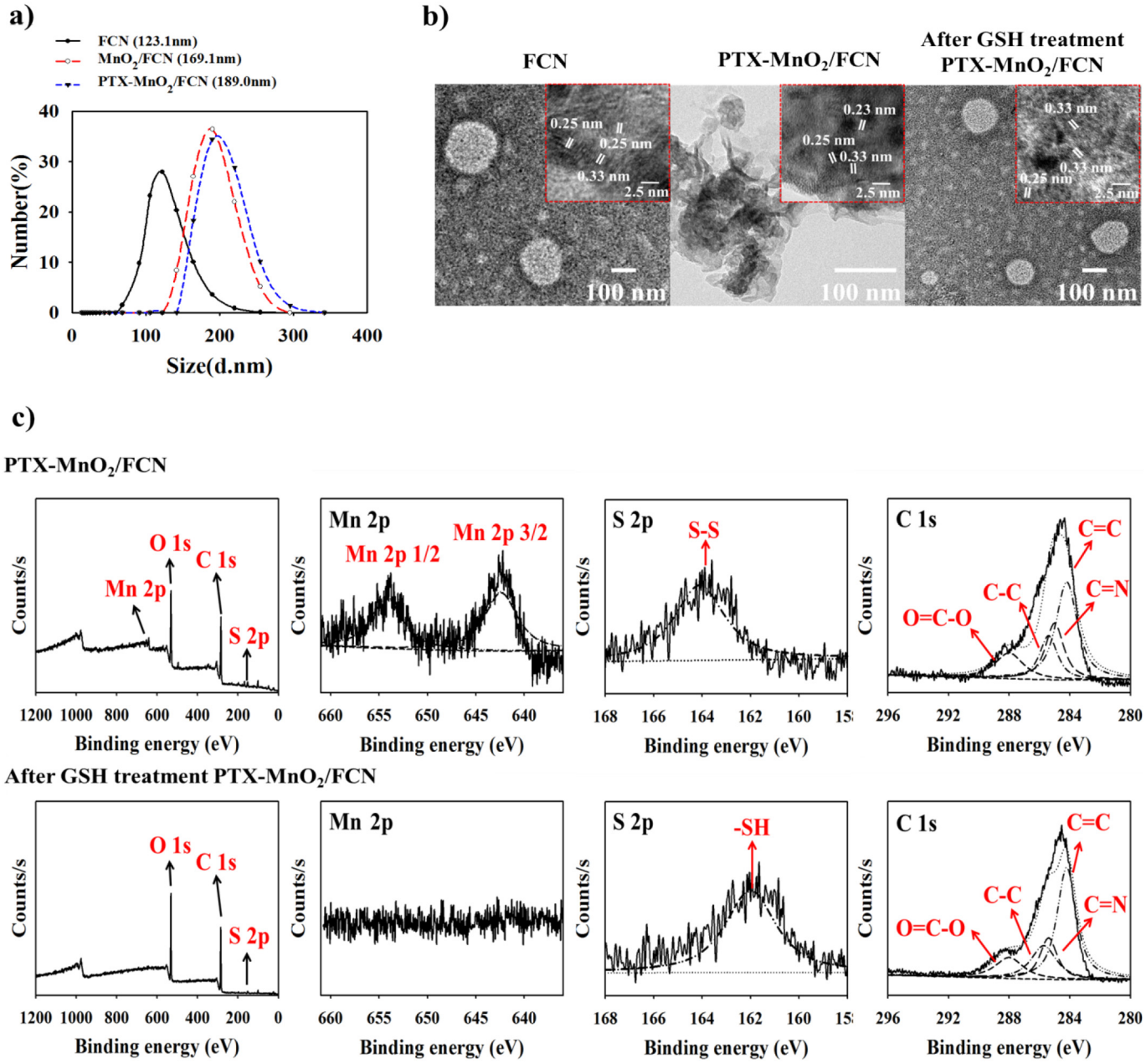

Fig. 2. (a) Dynamic light scattering measurement of FCN, MnO_2/FCN, and PTX-MnO_2/FCN (concentration of 1 mg/mL). (b) Transmission electron microscopy of FCN (left), PTX-MnO_2/FCN (middle), and 10 mM GSH-treated PTX-MnO_2/FCN (right). (c) X-ray photoelectron spectroscopy survey scan of Mn 2p, S 2p, C 1s, spectra before and after GSH treatment.

demonstrated specific targeting to CD44 receptors and showed high fluorescence intensity, which was quenched at a wavelength of 360–600 nm owing to the attachment of MnO_2 nanosheets. The uptake of PTX-MnO_2/FCN depended on HA mobility and attachment to the CD44 receptor, which in this case was hindered by the MnO_2 nanosheet. Treatment with 10 mM GSH resulted in the reduction of the MnO_2 nanosheet to Mn^{2+}, and this exposed the FCN inside the PTX-MnO_2/FCN. The mobility of FCN was recovered, evident by the increased cellular uptake of MDCK and MDA-MB-231 (Fig. 4(d) and (e)) (Shu et al., 2018). A stronger fluorescence intensity was observed in MDA-MB-231 treated cells (Fig. 4(e)), A stronger fluorescence intensity was observed in MDA-MB-231 treated cells (Fig. 4(e)), which was due to the selective targeting of HA and the overexpressed CD44 receptor on cancer cells, as compared to MDCK cells (Fig. 4(d)) (Yang et al., 2015; Zhang et al., 2018).

3.3. Cytotoxicity assay and confocal imaging of PTX-MnO_2/FCN

To investigate the biocompatibility and toxicity of the particles, the MTT cell viability assay was performed with MDCK and MDA-MB-231 cells. MnO_2/FCN showed good biocompatibility with both cells at concentrations ranging from 0.001 to 1 mg/mL in the absence or presence of GSH (Fig. 5(a)). After the loading of PTX, MDA-MB-231 cell viability was reduced to 20% in the presence of 1 mg/mL PTX-MnO_2/FCN and 0 mM GSH, while MDCK cells retained good viability. However, the treatment of both cell types with 10 mM GSH resulted in decreased viability due to the release of PTX, which was toxic to both normal cells and tumor cells. To further confirm these effects, the live/dead cell analysis was conducted after the treatment of cells with 1 mg/mL PTX-MnO_2/FCN, as was used for the MTT assay. MDCK and MDA-MB-231 cells survived (green color) after the treatment with MnO_2/FCN in the presence of 0 and 10 mM GSH (Fig. 5(b)), indicative of the

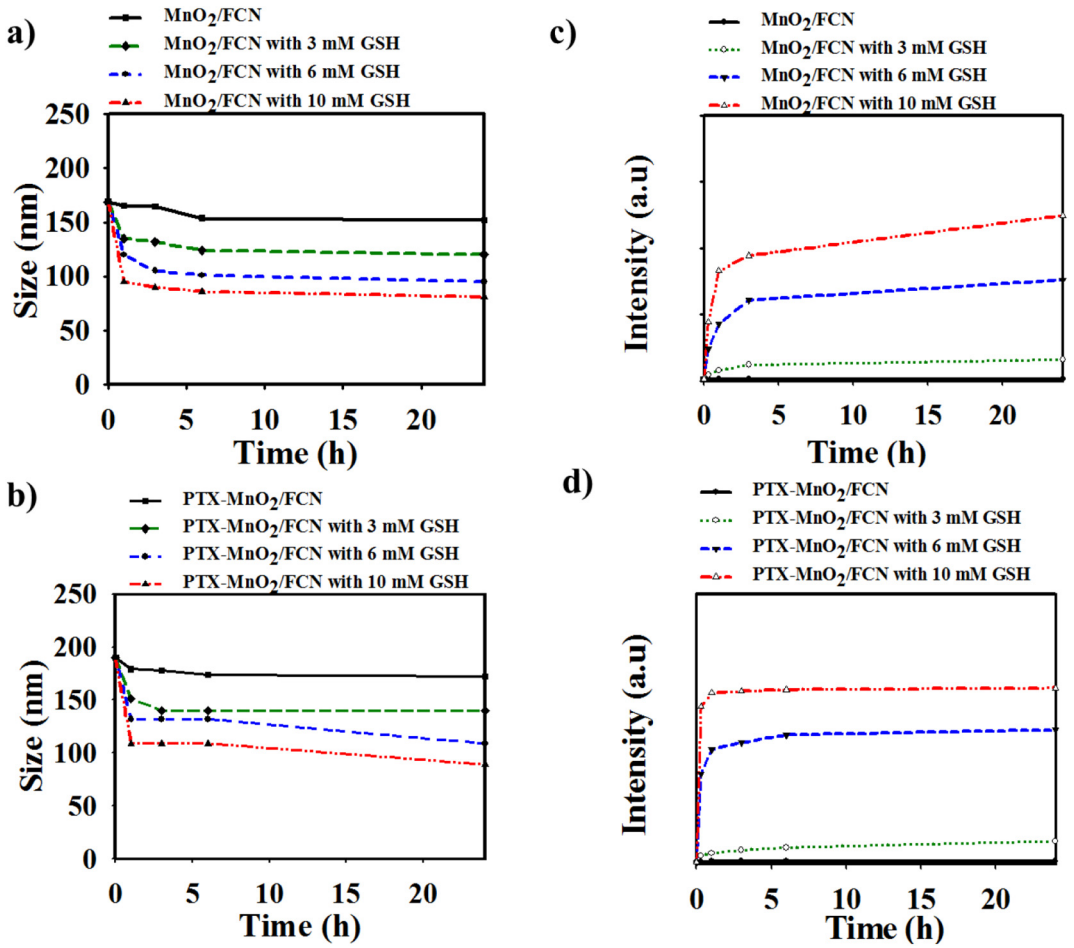

Fig. 3. Dynamic light scattering histograms of (a) MnO_2/FCN and (b) PTX-MnO_2/FCN at different concentrations of GSH. Time-dependent fluorescence emission intensities of (c) MnO_2/FCN and (d) PTX-MnO_2/FCN at different GSH concentrations (n = 3).

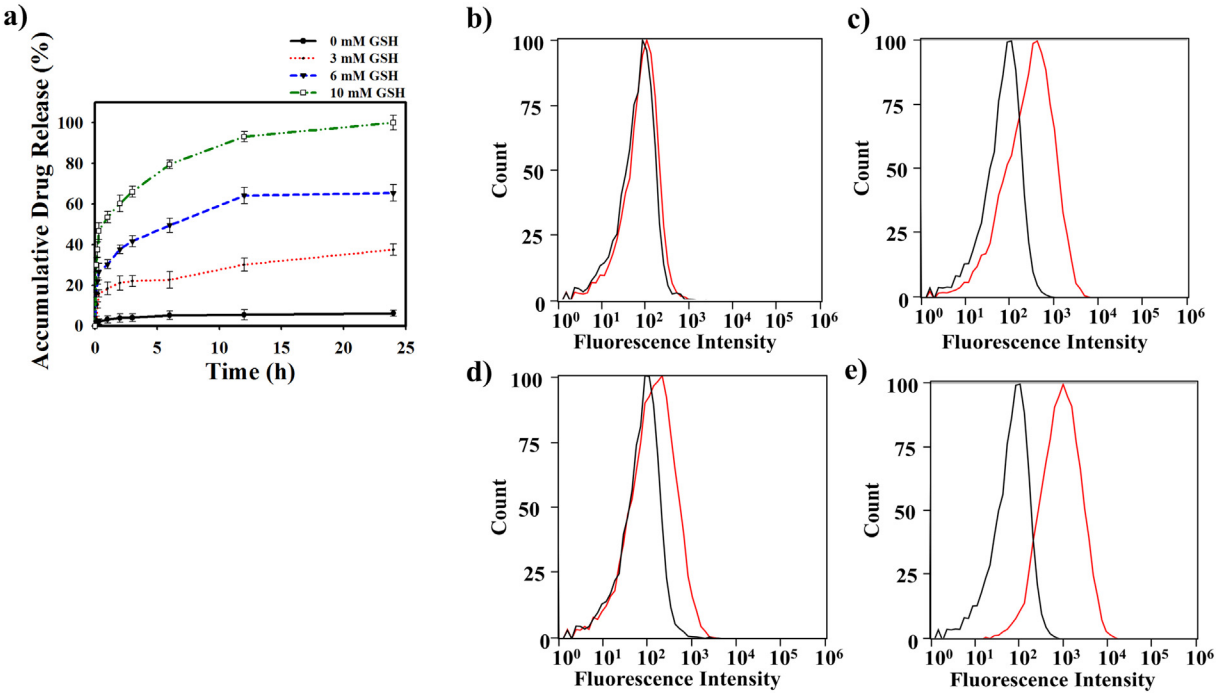

Fig. 4. (a) *In vitro* release profile of PTX from PTX-MnO_2/FCN at different concentrations of GSH in PBS (pH 7.4). Flow cytometry analysis of the cellular uptake of PTX-MnO_2/FCN in MDCK and MDA-MB-231 cells before (b and c) and after treatment with 10 mM glutathione (d and e).

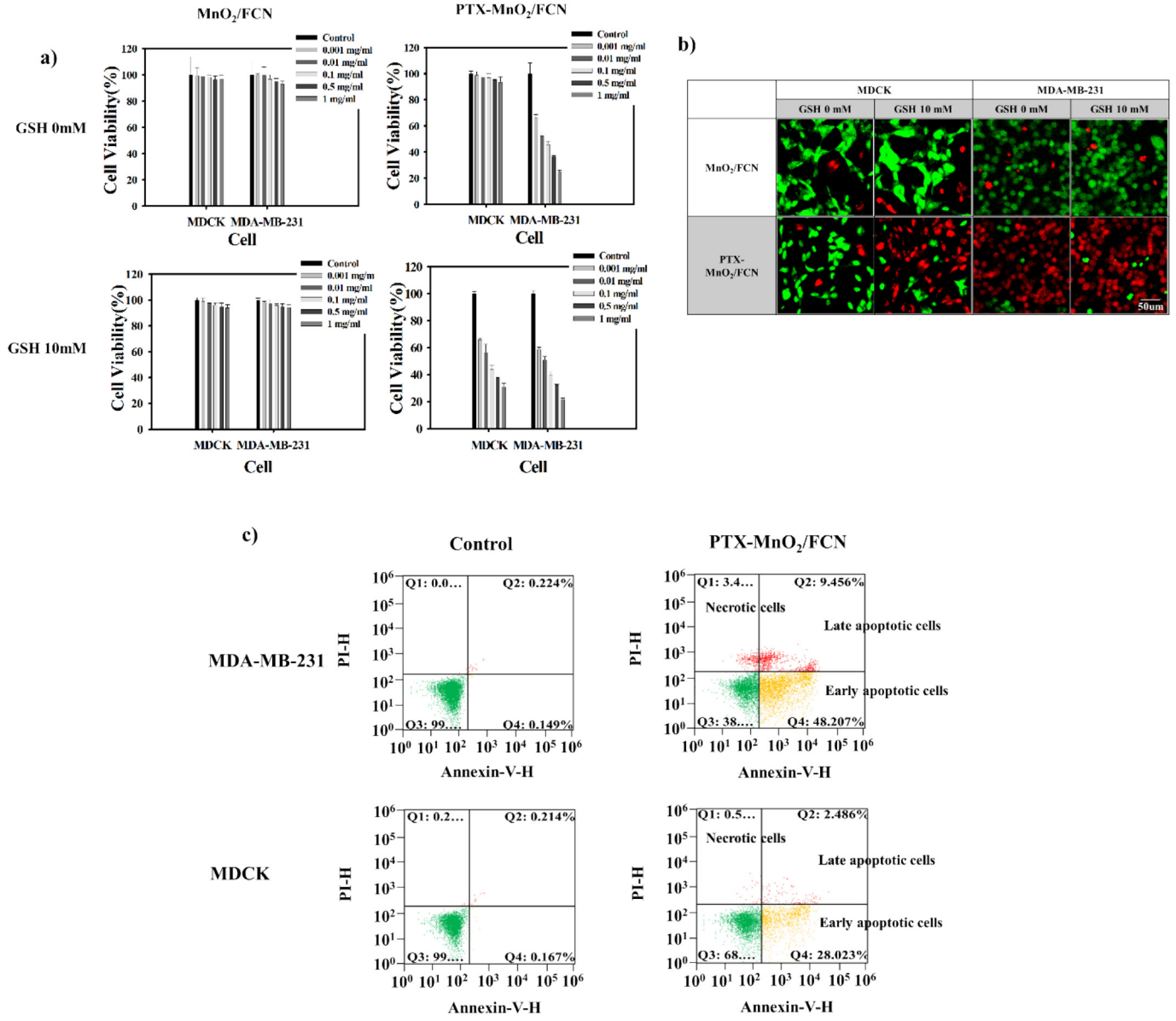

Fig. 5. (a) MTT assay of *in vitro* viability of MDCK and MDA-MB-231 cells treated with PTX-MnO_2/FCN in the presence of GSH. (b) Live and dead cell imaging. (c) Flow cytometry of cell apoptosis after PTX-MnO_2/FCN uptake (control: cells in PBS solution without PTX-MnO_2/FCN, $n = 3$).

good biocompatibility of the system. The therapeutic effect of PTX-MnO_2/FCN in MDA-MB-231 cells is displayed in Fig. 5(b). Most of the cancer cells were dead (red color) in the absence and presence of 10 mM GSH. The results were confirmed by flow cytometry detection of cell apoptosis using Annexin-V/PI staining (Lien et al., 2013). As shown in Fig. 5(c), PTX-loaded into the drug delivery matrix increased the population of cells in the early and late stages of apoptosis. The uptake of PTX-MnO_2/FCN by cells resulted in an increase in the number of MDCK cells in early and late apoptosis from 0.167% and 0.214% to 28.023% and 2.486%, respectively, reflecting the toxicity of PTX. MDA-MB-231 cancer cell populations displayed higher numbers of cells in early and late apoptosis stage (from 0.149% and 0.224% to 48.207% and 9.456%, respectively) than did MDCK cell populations. In addition, the percentage of necrotic cells increased from 0% to 3.4%, indicating that our DDS had excellent selectivity and is suitable for anticancer therapy.

Due to MDA-MB-231intracellular GSH concentration, the cells incubated with PTX-MnO_2/FCN emitted fluorescence whether in the presence and absence of environment GSH as shown in Fig. S3. MDA-MB-231 breast cancer cells, which contain higher concentrations of GSH than MDCK cells, only emitted fluorescence after treatment with 10 mM GSH. Confocal imaging showed that the cellular internalization and imaging properties of PTX-MnO_2/FCN were different over time in MDA-MB-231 cells (Fig. 6). The internalization of PTX-MnO_2/FCN was investigated using LysoTracker Green (lysosomal compartment) and SYTO 61 (nucleus) staining by the merged signal between the marker and the carbon nanogel (Zhitomirsky et al., 2018; Wlodkowic et al., 2008; Fan et al., 2012). In the first 30 min, PTX-MnO_2/FCN displayed a weak fluorescence signal because of the limited uptake of PTX-MnO_2/FCN by MDA-MB-231 cells. The fluorescence intensity continuously increased thereafter in association with the high concentration of GSH in cancer cells, indicating that the nanomaterial had already accumulated inside the cells. However, the internalization was reduced due to the escape of the drug carrier from liposomal vesicles into the cytoplasm, which gradually diminished the fluorescence signal between 4 h and 6 h (Choi et al., 2018; Thompson et al., 2012).

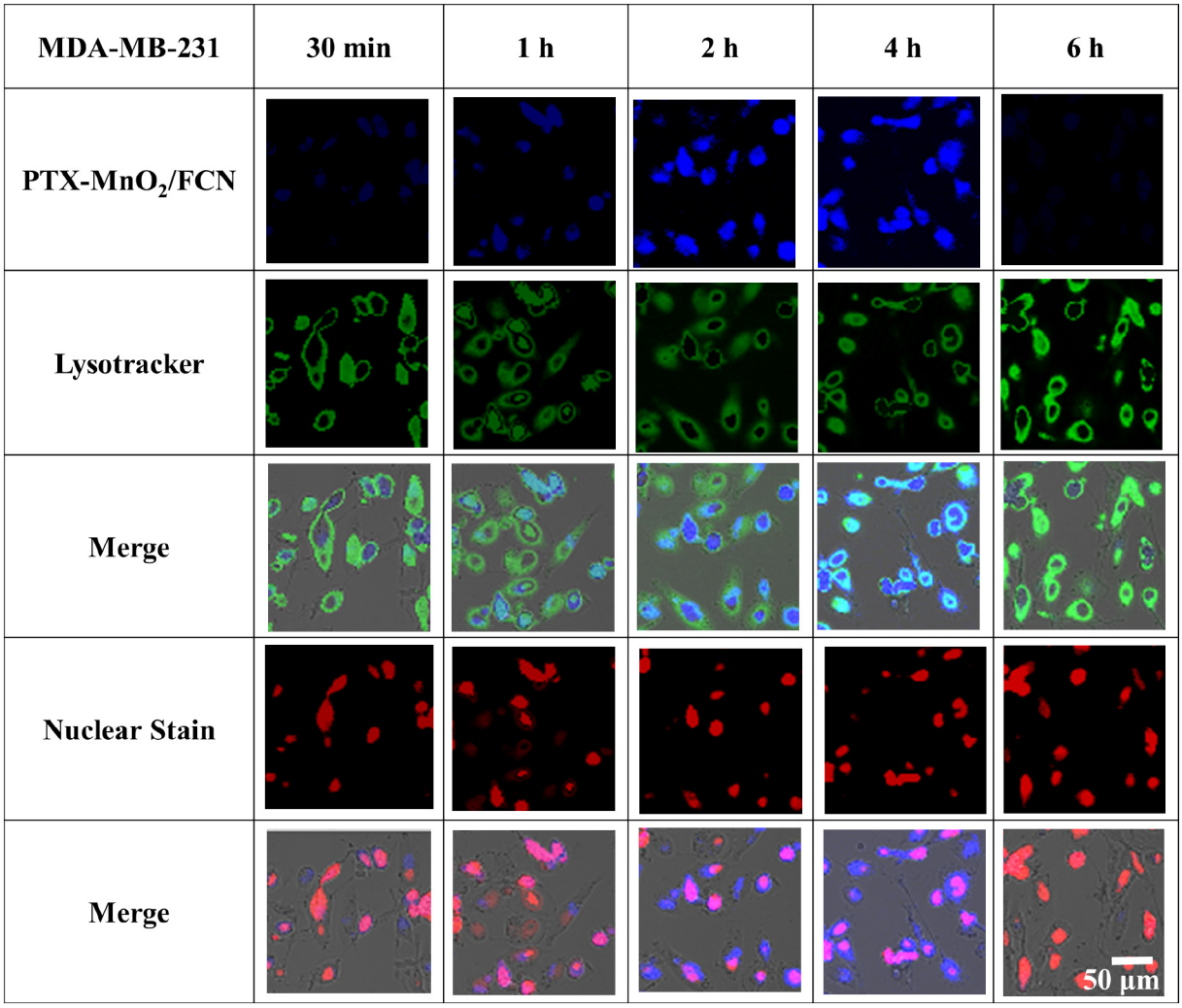

Fig. 6. Confocal imaging of MDA-MB-231 cells incubated with PTX-MnO_2/FCN for 0.5, 1, 2, 4, and 6 h (1 mg/mL). PTX-MnO_2/FCN (blue); lysosomes (Lysotracker, green); nucleus (SYTO 61, red). Scale bars indicate 50 μm. (For interpretation of the references to color in this figure legend, the reader is referred to the web version of this article.)

4. Conclusion

In this study, we demonstrate the successful synthesis of a PTX-loaded redox-responsive FCN based on *in situ* carbonized HA as a breast cancer cell-targeting and bioimaging system. The DDS matrix avoids issues of premature drug release after entering the human bloodstream under normal conditions, reflecting the presence of disulfide bonds and MnO_2 attachment that respond only to high redox potential. PTX-MnO_2/FCN selectively delivers the drug to cancer cells and initiates the therapeutic process by opening the structure and releasing the drug in response to a high GSH level. The fluorescence nanogel shows excellent biocompatibility and specific targeting properties to tumor cells without any significant impact on normal cells. PTX-MnO_2/FCN exhibits stable fluorescence intensity after GSH treatment, indicative of its potential as a biosensor. Despite the advantages for bioimaging, this system will more suitable for trigger-induced use if it can differentiate between tumor and normal cells due to the change in the fluorescence color in response to GSH. Additional electrochemical characterization is needed to improve the detection properties of the system, along with a preferable limit of detection value. Finally, the newly developed PTX-MnO_2/FCN as a smart DDS is a potentially valuable redox-responsive bioimaging material with simultaneous therapeutic properties for medical applications.

Conflicts of interest

The authors declare that they have no competing financial interests.

Acknowledgements

This research was supported by Grant No. 10062079 from the Ministry of Trade, Industry and Energy (MOTIE) and the Basic Science Research Program through the National Research Foundation of Korea (NRF) funded by the Ministry of Education (NRF-2017R1A2B2002365 and 2018R1A6A1A03023788).

Appendix A. Supplementary data

Supplementary data to this article can be found online at https://doi.org/10.1016/j.ejps.2019.04.027.

References

Al-Nahain, A., Nam, J.A., Mok, H., Lee, Y.K., Park, S.Y., 2013. Dual-responsive cross-linked pluronic micelles as a carrier to deliver anticancer drug taxol. Macromol. Res. 21, 92–99.

An, B.K., Kwon, S.K., Jung, S.D., Park, S.Y., 2002. Enhanced emission and its switching in fluorescent organic nanoparticles. J. Am. Chem. Soc. 124, 14410–14415.

Cabeza, L., Ortiz, R., Prados, J., Delgado, Á.V., Martin-Villena, M.J., Clares, B., Perazzoli,

G., Entrena, J.M., Melguizo, C., Arias, J.L., 2017. Improved antitumor activity and reduced toxicity of doxorubicin encapsulated in poly(ε-caprolactone) nanoparticles in lung and breast cancer treatment: an in vitro and in vivo study. Eur. J. Pharm. Sci. 102, 24–34.
Castner, D.G., 1996. X-ray photoelectron spectroscopy sulfur 2p study of organic thiol and disulfide binding interactions with gold surfaces. Langmuir 12, 5083–5086.
Chen, Y., Ye, D., Wu, M., Chen, H., Zhang, L., Shi, J., Wang, L., 2014. Break-up of two-dimensional MnO_2 nanosheets promotes ultrasensitive pH-triggered theranostics of cancer. Adv. Mater. 26, 7019–7026.
Chen, S., Bian, Q., Wang, P., Zheng, X., Lv, L., Dang, Z., Wang, G., 2017. Photo, pH, and redox multi-responsive nanogels for drug delivery and fluorescence cell imaging. Polym. Chem. 8, 6150–6157.
Choh, S.Y., Cross, D., Wang, C., 2011. Facile synthesis and characterization of disulfide-crosslinked hyaluronic acid hydrogels for protein delivery and cell encapsulation. Biomacromolecules 12, 1126–1136.
Choi, C.A., Lee, J.E., Mazrad, Z.A.I., In, I., Jeong, J.H., Park, S.Y., 2018. Redox- and pH-responsive fluorescent carbon nanoparticles-MnO_2-based FRET system for tumor-targeted drug delivery *in vivo* and *in vitro*. J. Ind. Eng. Chem. 63, 208–219.
Chowdhuri, A.R., Tripathy, S., Haldar, C., Roy, S., Sahu, S.K., 2015. Single step synthesis of carbon dot embedded chitosan nanoparticles for cell imaging and hydrophobic drug delivery. J. Mater. Chem. B 3, 9122–9131.
Dai, X., Cheng, H., Bai, Z., Li, L., 2017. Breast cancer cell line classification and its relevance with breast tumor subtyping. J. Cancer 8 (16), 3131–3141.
Danaei, M., Dehghankhold, M., Ataei, S., Davarani, F.H., Javanmard, R., Dokhani, A., Khorasani, S., Mozafari, M.R., 2018. Impact of particle size and polydispersity index on the clinical applications of lipidic nanocarrier systems. Pharmaceutics 10, 57.
Ding, C., Zhu, A., Tian, Y., 2014. Functional surface engineering of C-dots for fluorescent biosensing and *in vivo* bioimaging. Acc. Chem. Res. 47, 20–30.
Fan, F., Nie, S., Yang, D., Luo, M., Shi, H., Zhang, Y.H., 2012. Labeling lysosomes and tracking lysosome-dependent apoptosis with a cell-permeable activity-based probe. Bioconjug. Chem. 23, 1309–1317.
Ghaffaro, M., Gholamreza, D., Abedi-Gaballu, F., Kashanian, S., Baradaran, B., Dolatabadi, J.E.N., Losic, D., 2018. Surface functionalized dendrimers as controlled-release delivery nanosystems for tumor targeting. Eur. J. Pharm. Sci. 122, 311–330.
Gupta, A.S., 2016. Role of particle size, shape, and stiffness in design of intravascular drug delivery systems: insights from computations, experiments, and nature. Wiley Interdiscip. Rev. Nanomed. Nanobiotechnol. 8, 255–270.
Hu, Y., Du, Y., Liu, N., Liu, X., Meng, T., Cheng, B., He, J., You, J., Yuan, H., Hu, F., 2015a. Selective redox-responsive drug release in tumor cells mediated by chitosan based glycolipid-like nanocarrier. J. Control. Release 206, 91–100.
Hu, Y.W., Du, Y.Z., Liu, N., Liu, X., Meng, T.T., Cheng, B.L., He, J.B., You, J., Yuan, H., Hu, F.Q., 2015b. Selective redox-responsive drug release in tumor cells mediated by chitosan based glycolipid-like nanocarrier. J. Control. Release 206, 91–100.
Huang, Y., Yao, X., Zhang, R., Ouyang, L., Jiang, R., Liu, X., Song, C., Zhang, G., Fan, Q., Wang, L., Huang, W., 2014. Cationic conjugated polymer/fluoresceinamine-hyaluronan complex for sensitive fluorescence detection of CD44 and tumor-targeted cell imaging. ACS Appl. Mater. Interfaces 6, 19144–19153.
Kang, E.B., In, I., Lee, K.D., Park, S.Y., 2017. Mitochondria-targeted fluorescent carbon-nanoplatform for NIR-triggered hyperthermia and mitochondrial inhibition. J. Ind. Eng. Chem. 55, 224–233.
Kim, S.H., In, I., Park, S.Y., 2017. pH-responsive NIR-absorbing fluorescent polydopamine with hyaluronic acid for dual targeting and synergistic effects of photothermal and chemotherapy. Biomacromolecules 18, 1825–1835.
Kim, Y.K., Lee, J.E., Ryplida, B., Choi, C.A., Mazrad, Z.A.I., Lee, G., Lee, S., In, I., Jeong, J.H., Park, S.Y., 2018. Redox-responsive FRET-based polymer dot with BODIPY for fluorescence imaging-guided chemotherapy of tumor. Eur. J. Pharm. Biopharm. 132, 200–210.
Kong, T., Hao, L., Wei, Y., Cai, X., Zhu, B., 2018. Doxorubicin conjugated carbon dots as a drug delivery system for human breast cancer therapy. Cell Prolif. 51, e12488.
Li, Y., Xiao, K., Luo, J., Xiao, W., Lee, J.S., Gonik, A.M., Kato, J., Dong, T., Lam, K.S., 2011. Well-defined reversible disulfide cross-linked micelles for on-demand paclitaxel delivery. Biomaterials 32, 6633–6645.
Liaskoni, A., Angelopoulou, A., Voulgari, E., Popescu, M., Tsitsilianis, C., Avgoustakis, K., 2018. Paclitaxel controlled delivery using a pH-responsive functional-AuNP/block-copolymer vesicular nanocarrier composite system. Eur. J. Pharm. Sci. 117, 177–186.
Lien, S.C., Chang, S.F., Lee, P.L., Wei, S.W., Chang, M.D.T., Chang, J.Y., Chiu, J.J., 2013. Mechanical regulation of cancer cell apoptosis and autophagy: roles of bone morphogenic protein receptor, Smad1/5, and p38 MAPK. Biochim. Biophys. Acta 1833, 3124–3133.
Mazrad, Z.A.I., Phuong, P.T.M., Choi, C.A., Insik, I., Lee, K.D., Park, S.Y., 2018. pH/redox-triggered photothermal treatment for cancer therapy based dual-responsible cationic polymer dot. ChemMedChem 13, 2437–2447.
Meng, F., Hennink, W.E., Zhong, Z., 2009. Reduction-sensitive polymers and bioconjugates for biomedical applications. Biomaterials 30, 2180–2198.
Ossipov, D.A., Piskounova, S., Varghese, O.P., Hilborn, J., 2010. Functionalization of hyaluronic acid with chemoselectivity groups via a disulfide-based protection strategy for in situ formation of mechanically stable hydrogels. Biomacromolecules 11, 2247–2254.
Ou, M., Huang, J., Yang, X., Quan, K., Yang, Y., Xie, N., Wang, K., 2017. MnO_2 nanosheet mediated "DD–A" FRET binary probes for sensitive detection of intracellular mRNA. Chem. Sci. 8, 668–673.
Pedrosa, S.S., Gonçalves, C., David, L., Gama, M., 2014. A novel crosslinked hyaluronic acid nanogel for drug delivery. Macromol. Biosci. 14, 1556–1568.
Peng, Z., Li, S., Han, X., Al-Youbi, A.O., Bashammakh, A.S., El-Shahawi, M.S., Leblanc, R.M., 2016. Determination of the composition, encapsulation efficiency and loading capacity in protein drug delivery systems using circular dichroism spectroscopy. Anal. Chim. Acta 937, 113–118.
Sharker, S.M., Kim, S.M., Lee, J.E., Jeong, J.H., In, I., Lee, K.D., Lee, H., Park, S.Y., 2015. *In situ* synthesis of luminescent carbon nanoparticles toward target bioimaging. Nanoscale 7, 5468–5475.
Shu, F., Lv, D., Song, X.L., Huang, B., Wang, C., Yu, Y., Zhao, S.C., 2018. Fabrication of a hyaluronic acid conjugated metal organic framework for targeted drug delivery and magnetic resonance imaging. RSC Adv. 8, 6581–6589.
Smith, S.M., Cai, L., 2012. Cell specific CD44 expression in breast cancer requires the interaction of AP-1 and NFκB with a novel cis-element. PLoS One 7, e50867.
Sun, X., Lei, Y., 2017. Fluorescent carbon dots and their application. TrAC Trends Anal. Chem. 89, 163–180.
Thompson, D.B., Villaseñor, R., Dorr, B.M., Zerial, M., Liu, D.R., 2012. Cellular uptake mechanisms and endosomal trafficking of supercharged proteins. Chem. Biol. 19, 831–843.
Tripodo, G., Trapani, A., Torre, M.L., Giammona, G., Trapani, G., Mandracchia, D., 2015. Hyaluronic acid and its derivatives in drug delivery and imaging: recent advances and challenges. Eur. J. Pharm. Biopharm. 97, 400–416.
Wang, Y., Jiang, K., Zhu, J., Zhang, L., Lin, H., 2015. A FRET-based carbon-dot MnO_2 nanosheets architecture for glutathione sensing in human whole blood samples. Chem. Commun. 51, 12748–12751.
Wang, X., Gu, X., Wang, H., Yang, J., Mao, S., 2018. Enhanced delivery of doxorubicin to the liver through self-assembled nanoparticles formed via conjugation of glycyrrhetinic acid to the hydroxyl group of hyaluronic acid. Carbohydr. Polym. 195, 170–179.
Wlodkowic, D., Skommer, J., Darzynkiewicz, Z., 2008. SYTO probes in the cytometry of tumor cell death. Cytometry A 73A, 496–507.
Yang, C., He, Y., Zhang, H., Liu, Y., Wang, W., Du, Y., Gao, F., 2015. Selective killing of breast cancer cells expressing activated CD44 using CD44 ligand-coated nanoparticles *in vitro* and *in vivo*. Oncotarget 6 (17), 15283–15296.
Youm, I., Agrahari, V., Murowchick, J.B., Youn, B.C., 2014. Uptake and cytotoxicity of docetaxel-loaded hyaluronic acid-grafted oily core nanocapsules in MDA-MB 231 cancer cells. Pharm. Res. 31 (9), 2439–2452.
Zhang, Z., Feng, S.S., 2006. The drug encapsulation efficiency, *in vitro* drug release, cellular uptake and cytotoxicity of paclitaxel-loaded poly(lactide)–tocopheryl polyethylene glycol succinate nanoparticles. Biomaterials 27, 4025–4033.
Zhang, Y., Wu, K., Sun, H., Zhang, J., Yuan, J., Zhong, Z., 2018. Hyaluronic acid-shelled disulfide-cross-linked nanopolymersomes for ultrahigh-efficiency reactive encapsulation and CD44-targeted delivery of mertansine toxin. ACS Appl. Mater. Interfaces 10 (2), 1597–1604.
Zhitomirsky, B., Farber, H., Assaraf, Y.G., 2018. LysoTracker and MitoTracker Red are transport substrates of P-glycoprotein: implications for anticancer drug design evading multidrug resistance. J. Cell. Mol. Med. 22, 2131–2141.